A Model and Regularization Scheme for Ultrasonic Beamforming Clutter Reduction

Brett Byram, *Member, IEEE*, Kazuyuki Dei, *Student Member, IEEE*, Jaime Tierney, Douglas Dumont, *Member, IEEE*

Abstract

Acoustic clutter produced by off-axis and multipath scattering is known to cause image degradation, and in some cases these sources may be the prime determinants of *in vivo* image quality. We have previously shown some success addressing these sources of image degradation by modeling the aperture domain signal from different sources of clutter, and then decomposing aperture domain data using the modeled sources. Our previous model had some shortcomings including model mismatch and failure to recover B-Mode speckle statistics. These shortcomings are addressed here by developing a better model and by using a general regularization approach appropriate for the model and data. We present results with L1 (lasso), L2 (ridge) and L1/L2 combined (elastic-net) regularization methods. We call our new method Aperture Domain Model Image REconstruction (ADMIRE).

Our results demonstrate that ADMIRE with L1 regularization or weighted towards L1 in the case of elastic-net regularization have improved image quality. L1 by itself works well, but additional improvements are seen with elastic-net regularization over the pure L1 constraint. On *in vivo* example cases, L1 regularization showed mean contrast improvements of 4.6 dB and 6.8 dB, on fundamental and harmonic images, respectively. Elastic net regularization ($\alpha = 0.9$) showed mean contrast improvements of 17.8 dB on fundamental images and 11.8 dB on harmonic images. We also demonstrate that in uncluttered Field II simulations the decluttering algorithm produces the same contrast, contrast-to-noise ratio and speckle signal-to-noise ratio as normal B-Mode imaging, demonstrating that ADMIRE preserves typical image features.

I. Introduction

Ultrasound's low-cost and convenience make it the most widely used advanced clinical imaging modality in the United States [1]. Unfortunately, ultrasound's broad utility belies its quality in many real clinical instances where most exams are subjected to at least some level of image degradation and many fail altogether [2]–[6]. Often poor image-quality is attributable to penetration and resolution limitations, but acoustic clutter may be the most significant and widespread cause of image degradation [7].

Acoustic clutter is something of a catch-all term for non-diffraction limited image degradation, which includes multipath scattering, off-axis scattering and phase-aberration induced degradation of the point spread function. A number of methods have been proposed to suppress these sources of degradation including correcting temporal wavefront distortions e.g. phase-aberration correction [8]–[10], standard and adaptive apodization schemes [11]–[15], and harmonic imaging [16]–[18]. With the exception of harmonic imaging, these techniques have had only mixed clinical success.

While most beamforming methods in the literature have focused on restoring, optimizing or surpassing diffraction limited beamforming, suppressing multipath scattering has also been explored. A number of methods exist, but again harmonic imaging is the one that is the most clinically impactful [7], [16], [17]; although, it still does not eliminate all clutter [19]. Time reversal is a classic method for suppressing multipath scattering if a point target or a rapidly changing speckle pattern are available [20], [21], but it is harder to apply to attenuating media [22]. There are also several new methods that suppress multipath clutter. One new method is second-order ultrasound field (SURF) imaging, which takes advantage of nonlinear wave propagation by directly manipulating nonlinear propagation in a way that specifically targets the multipath scattering problem [19], [23]–[25]. SURF imaging is promising, but it may be some time before the necessary high-bandwidth transducers and arbitrary transmitters are readily available [19]. A second set of new methods are the aperture domain coherence based beamformers, which include short-lag spatial coherence imaging [26]–[29]. These methods suppress off-axis and multipath scattering and have translated very well to *in vivo* scenarios. Their biggest challenge may be that they create fundamentally different images compared to normal B-Mode images, which may hinder clinical adoption. Aperture domain coherence methods also eliminate the radio frequency (RF) signal making them unsuitable for estimating displacement using conventional high-quality methods.

In order to address the problem of both multipath and off-axis clutter sources, we recently proposed a new model-based approach [30]. The primary goal of the approach is to preserve the ultrasound channel data (or RF data), while minimizing acoustic clutter. A secondary goal is to develop a tool that can characterize the spatial distribution of clutter from *in vivo* data. The method relies on linearizing the problem of multipath scattering by ignoring multipath propagation and considering multiple scattering as time-delayed wavefronts arriving from depths shallow to the normal region of interest. The initial model

The authors are with the department of Biomedical Engineering at Vanderbilt University, Nashville, TN, USA. e-mail: brett.c.byram@vanderbilt.edu.
The authors would like to acknowledge NIH grant 1S10RR026828.

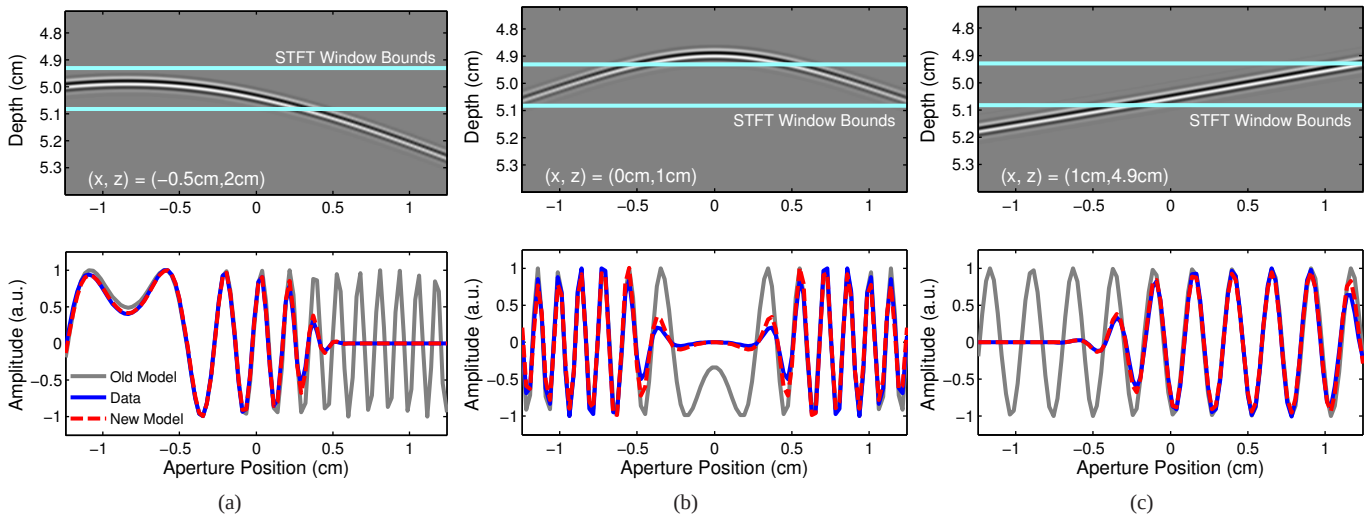

(a) (b) (c)

Fig. 1: Three examples are shown for the time-domain channel data and the corresponding aperture domain data after the STFT has been applied axially. The examples show several cases of x_n, z_n, and τ_n for a region of interest centered about 5 cm. Comparisons are made between the data, the new model and the old model in each of the bottom graphs.

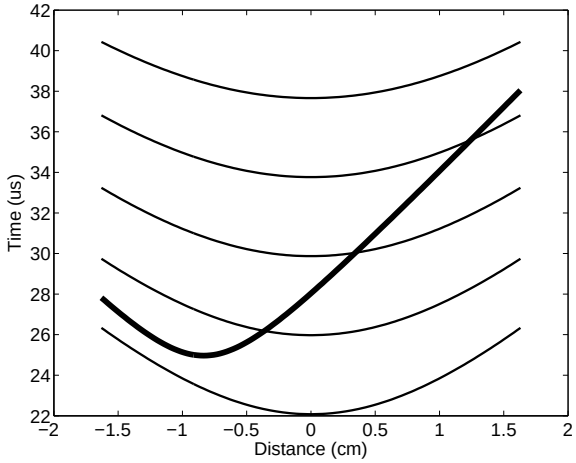

Fig. 2: When multipath scattering does occur the wavefront will extend across multiple dynamic receive delay profiles. This is demonstrated in the graph above with several receive delay profiles shown as thin lines, and a wavefront delay profile from modeled multipath scattering shown as a black line.

of this linearization applied the Fresnel approximation so that the signal sampled by a transducer array could be modeled as a summation of linear frequency modulated sinusoids,

$$p_s(x;t,\omega) \approx \sum_{n=0}^{N-1} A_n e^{jg_n x^2 + jk_n x + j\phi_n} \tag{1}$$

where

$$g_n = \frac{kz_n}{2z_f(z_f - z_n)}, \quad \text{and } k_n = \frac{-x_n k}{z_f - z_n},$$

and where each N is a scattering source at location (x_n, z_n) encoded by the chirp-rates, g_n, and frequencies, k_n. z_f is the depth of the signal of interest, and k is the wavenumber. By using this model to decompose a signal into its scattering sites and reconstructing only the signals from the region of interest, we demonstrated image quality improvements. Specifically, the method demonstrated significant improvements in contrast, but little change in contrast-to-noise ratio (CNR) on average. This seemingly paradoxical result was probably caused by the lower speckle signal-to-noise ratio (SNR) compared to normal B-mode imaging. In order to address these shortcomings and several open questions from the previous work, we present a new model and decomposition scheme, which we call Aperture Domain Model Image Reconstruction (ADMIRE).

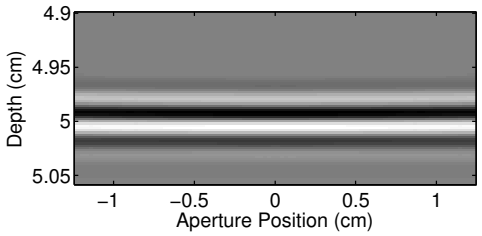

(a) γ=0

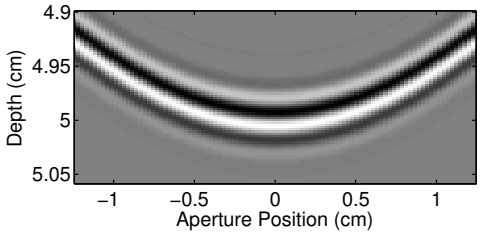

(b) γ=-0.5

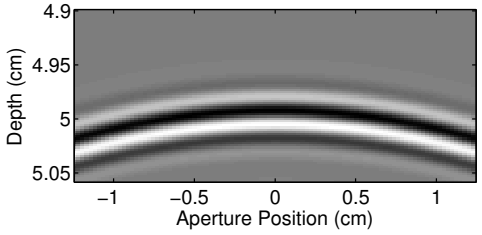

(c) γ=0.5

Fig. 3: Three examples are shown for different dynamic receive γ scales. When γ is negative the dynamic receive foci are shallower than normal so the wavefront becomes inverted, and when γ is positive the curvature from path-length differences is not entirely removed so some of the original curvature remains.

II. Methods

A. Received Wavefront Model

In our previous model we made several approximations so that our model components were constant amplitude, linear-frequency-modulated sinusoids. The previous simplifications are ignored here, and the new model for ADMIRE incorporates

- the exact wavefront delay profile,
- the effect of dynamic receive beamforming on multipath sources,
- the impact of the axial short-time Fourier transform (STFT) window
- and element directional sensitivity.

The model incorporating these effects can be presented generically as

$$p_s(x;t,\omega) = \sum_{n=0}^{N-1} A(x;x_n,z_n,\tau_n,\omega)e^{jk\tau(x;x_n,z_n,\tau_n)}, \tag{2}$$

where k is the wavenumber, x is the aperture position, t and ω localize the signal in time and frequency, $\tau(x;x_n,z_n,\tau_n)$ is the wavefront delay for a signal arriving from point (x_n,z_n) at time τ_n and $A(x;x_n,z_n,\tau_n,\omega)$ is the lateral amplitude modulation induced by the STFT and the element sensitivity. $A(x;x_n,z_n,\tau_n,\omega)$ also depends on the signal's pulse shape and $\tau(x;x_n,z_n,\tau_n)$. The new model produces similar predictors as (1) but is no longer restricted to producing just linear, frequency-modulated sinusoids. Before preceding with a description of the various components of the model, several example wavefronts are shown in Fig. 1. The figure qualitatively compares new and old models against Field II simulated data to provide additional intuition and motivation for the new model.

To establish the specifics of (2), we first consider a scattered wavefront's arrival-time profile. For the typical free-space diffraction case, this is

$$\tau_{Diff}(x;x_n,z_n,\tau_n) = \frac{1}{c}\sqrt{(x-x_n)^2+z_n^2} + \tau_{n_0}. \tag{3}$$

Usually, τ_{n_0} would be defined as z_n/c, which models a ballistic wave propagating directly to the region of interest, scattering, and then propagating directly back to the array. However, τ_{n_0} is more general in our linearized representation of multipath

scattering. In our representation, τ_{n_0} can be any value within the receive duration of the ultrasound system, but practically, its value is limited based on the axial STFT window and the curvature for a given depth. We find it more convenient to define $\tau_{n_0} = \frac{1}{c}(2z_f - z_n) + \tau_n$, and then parameterize the model-space using τ_n.

Modeling the wavefront curvature from a given source location is straight forward and consistent with our previous approach. Here, we also introduce the impact of dynamic receive delays on the modeled wavefronts. In principal, applying dynamic receive delays is not necessary, but dynamically delaying the wavefronts and modeling this process has at least one clear benefit and another possible benefit. First, dynamic receive delays flatten the curvature of all wavefronts, including wavefronts resulting from multiple scattering. A flatter curvature means a wider segment of that wavefront falls within a given STFT window allowing for better estimation resolution. Second, dynamically delaying the wavefronts provides an opportunity to advantageously modulate the aperture domain signal to help better preserve the signal of interest[1].

First, we consider the impact of applying dynamic receive delays to wavefronts originating from multipath scattering. The problem is that wavefronts arriving from depths besides the intended focus have different curvatures than the corresponding receive delay profiles, and therefore these multiply scattered wavefronts traverse several different dynamic receive profiles, as illustrated in Fig. 2. To model this effect, the perceived depth of each part of the sampled wavefront needs to be computed so that the correct delays can be used in (2). To accomplish this, we start with the usual dynamic receive delays across the aperture and through depth,

$$\tau_{DR}(x; x_f, z_f) = \frac{1}{c}\sqrt{(x - x_f)^2 + z_f^2} + \frac{z_f}{c}, \tag{4}$$

where x is the aperture location and (x_f, z_f) are the dynamically updated focal locations. Next, we equate the multipath wavefront delays and the dynamic receive delays

$$\tau_{Diff}(x; x_n, z_n, \tau_n) = \tau_{DR}(x; x_f, z_f) \tag{5}$$

and solve for z_f. Purely by rearrangement, the result is

$$z_f(x) = \frac{d_0(x)^2 - (x_f - x)^2}{2d_0(x)}, \tag{6}$$

where

$$d_0(x) = \sqrt{(x - x_n)^2 + z_n^2} + c\tau_n.$$

Finally, the value for $z_f(x)$ can be inserted back into (4) to calculate the dynamic receive delay applied across each multiply scattered wavefront.

Next, we describe a method for intentionally modulating the aperture domain signal so that the primary region of interest is not near DC. The approach scales the depth dimension used for calculating the dynamic receive delay profile, which causes different receive delays than usual to be applied at a given depth. In this case, (4) is modified to

$$\tau_{DR_\gamma}(x; x_f, z_f) = \frac{1}{c}\sqrt{(x - x_f)^2 + ((1+\gamma)z_f)^2} + \frac{(1-\gamma)z_f}{c}, \tag{7}$$

and to extend to the multipath wavefront we again solve for $z_f(x)$ using (5) to obtain

$$\begin{aligned} z_f(x) =& \frac{d_0(x)(1-\gamma)}{4\gamma} \times \\ & (1 + \text{sgn}(\gamma)\sqrt{1 - 4\frac{\gamma((x - x_n)^2 - d_0(x)^2)}{d_0(x)^2(1-\gamma)^2}}), \end{aligned} \tag{8}$$

where γ is the scaling factor for the depth. As defined, negative γ creates curvatures corresponding to depths shallow to the usual focus, and the reverse for positive γ. Examples of the impact for several γ values on wavefront curvature are shown in Fig. 3.

The wavefront delays used in (2) are

$$\begin{aligned} \tau(x; x_n, z_n, \tau_n) = & \tau_{Diff}(x; x_n, z_n, \tau_n) - \\ & \tau_{DR}(x; x_f, z_f(x)) - (1+\gamma)\frac{z_f(x)}{c}. \end{aligned} \tag{9}$$

The wavefront delay is important for establishing the signal's phase across the aperture, but it is also important for calculating the amplitude modulation, $A(x)$, across the aperture. Using the modeled delay and an estimate of the pulse shape the lateral

[1]This is consistent with concepts in spectral estimation where the Cramer-Rao lower bound for a given frequency estimate is a function of that frequency [31]. Of note here is that for spectral estimation problems the Cramer-Rao bound for the DC estimation variance is incredibly poor. In the application considered here without an additional modulation, the wavefronts from the region of interest will be nearly DC signals.

amplitude modulation can be calculated as

$$A_{FT}^2(x) = \int_{t_c-\frac{\Delta t}{2}}^{t_c+\frac{\Delta t}{2}} w_{FT}^2(t-t_c) w_{env}^2(t-\tau(x;x_n,z_n,\tau_n))\,dt, \tag{10}$$

where Δt is the width of the STFT window, t_c is the center of the STFT window, w_{FT} is the window used for the STFT and w_{env} is the axial pulse envelope. For many relevant cases of w_{FT} and w_{env}, $A_{FT}(x)$ can be calculated analytically, but it is also possible to calculate $A_{FT}(x)$ from sampled realizations of w_{FT} and w_{env}. This second case may be useful for more exact representations of the pulse shape using empirical hydrophone measurements, or to adaptively estimate the pulse shape based on speckle statistics [32]. Here, for simplicity, we restrict ourselves to a rectangular window for w_{FT} and a Gaussian envelope for w_{env}. This lateral modulation resulting from STFT windowing does not describe all of the potential amplitude variation across the aperture.

We also include the effect of element sensitivity as described by Selfridge et al. and expressed as

$$A_{es}(x) = \frac{\sin(\frac{\pi w \sin(\theta)}{\lambda})}{\frac{\pi w \sin(\theta)}{\lambda}} \cos(\theta) \tag{11}$$

where $\theta = tan^{-1}(\frac{x-x_n}{z_n})$ [33]. Incorporating angular sensitivity is most important for shallow scatterers with high incidence angles of the received wavefront with transducer elements. Combining angular sensitivity with the STFT characteristics gives the amplitude modulation modeled here,

$$A_n(x) = A_{FT}(x) A_{es}(x). \tag{12}$$

The accuracy of the model was determined using Field II simulations with the parameters in Table I.

B. Model Space

Using our linearized scattering model for ADMIRE, we can express the signal received at a specific time as

$$y = X\beta, \tag{13}$$

where y is a single frequency of the observed channel data from a given STFT window location constructed as

$$y = [\Re\{S_w(x_i; mT, \omega_p)\}\ \Im\{S_w(x_i; mT, \omega_p)\}]^\top,$$

X is the model matrix of predictors constructed from (2),

$$X = \begin{bmatrix} \Re\{p_s(x;t,\omega)\}^\top & -\Im\{p_s(x;t,\omega)\}^\top \\ \Im\{p_s(x;t,\omega)\}^\top & \Re\{p_s(x;t,\omega)\}^\top \end{bmatrix},$$

and β contains the coefficients for the predictors in X. $\Re$ and $\Im$ denote the real and imaginary parts, respectively. The model matrix is formed by sampling the space from which scatterers are expected to return. There are many possible approaches to sampling the model space. Here, we identify a region ahead of time that will be the acceptance zone. Scatterers originating from within this zone will be used to reconstruct decluttered data, while scatterers outside this zone are discarded. In our experiments so far it is most efficient to sample the model space finely within the region of acceptance and sample the model more coarsely in the rejection zone.

We define the acceptance zone based on the expected resolution of a model predictor centered in the region of interest. The lateral resolution is calculated based on the bandwidth of the signal originating from the center of the region of interest, i.e. $res_{lat} \approx \lambda z \mathcal{F}\{|p_s(x;x_c,z_c,0)|\}_{BW}$, where $F\{|\cdot|\}_{BW}$ denotes the lateral bandwidth of the model predictor and (x_c, z_c) denotes the center of the region of interest. The axial resolution of the region of interest is approximated as $res_{axl} \approx 2res_{lat}$, and comes from work on parameter estimation of linear frequency modulated sinusoids [34]. The lateral and axial resolution are used to define an ellipsoidal acceptance region,

$$\left(\frac{x_n - x_r}{c_l res_{lat}}\right)^2 + \left(\frac{z_n - z_r}{c_a res_{axl}}\right)^2 \leq 1, \tag{14}$$

where c_l and c_a are scale factors selected to modify the size of the acceptance region, and x_r and z_r denote the center of the acceptance zone.

The sampling of the continuous parameter space of the ultrasound field can have a large outcome on the resulting decomposition. It is computationally advantageous to restrict the number of predictors in the model X, but an insufficiently populated model inhibits the ability of the model to suppress clutter and preserve the signal of interest. For all of the results here we have two different sampling grids depending on whether intentional receive modulation is used. For both sampling grids the "phase" parameter, tau_n is the same with a spacing of 0.0485λ in the acceptance region and 0.2423λ outside the acceptance zone. For the case of normal receive delays ($\gamma = 0$) the lateral and axial grid sampling inside the acceptance zone is $0.0668res_{lat}$ and $0.267res_{axl}$, respectively, and the sampling outside the acceptance zone is $1.34res_{lat}$ and $1.34res_{axl}$, respectively. For

the case of receive modulation with $\gamma = 0.5$ the sampling is finer. In this case the lateral and axial grid sampling within the acceptance region is $0.025res_{lat}$ and $0.10res_{axl}$, respectively. Outside the acceptance region the grid sampling is $0.5res_{lat}$ and $0.5res_{axl}$, respectively. For the purposes of image reconstruction a fixed grid is used throughout the image. This has the advantage of efficiency at the cost of increased decomposition error. For some applications not presented here it may be desirable to incorporate model selection and regularization tuning into a more robust cross-validation scheme, which is beyond the scope of this paper.

C. Decomposition and Regularization

Depending on the specific model-space sampling, the imaging sequence and the imaging depth, the ADMIRE model matrix could contain anywhere from several hundred predictors to over a million predictors. This is in contrast to the number of samples in the data vector, y, which will rarely have more than 256 elements for a 1D array. The massive difference between the number of data points and the number of model predictors presents a challenge. Ideally, estimating β could be accomplished by minimizing the squared error—$\hat{\beta} = (X^T X)^{-1} X^T y$, but this is ill-posed. To address this problem, additional constraints must be added in the form of regularization terms. Regularization schemes constraining the solution with L1 or L2 norms are typical. L1 is useful because it promotes coefficient sparsity, but the final solution will have fewer non-zero predictors than observations, and the predictors will be nearly (if not totally) uncorrelated. This property of L1 regularized model-fitting may be problematic for some *in vivo* ultrasound aperture-domain data sets because in many cases it will require multiple correlated model-predictors to reconstruct all scattering sources. Besides L1, the other typical scheme is L2 regularized model fitting. L2 is attractive because it allows for solutions with correlated model predictors, but while correlated predictors are useful, L2 performs coefficient shrinkage (not selection), so an L2 constrained solution may not have any coefficients equal to zero. Practically, this means that when using an L2 constraint for data originating from inside an anechoic cyst (i.e. no expected scattering from within the cyst), the model fit will almost always predict that there is scattering originating from the region of interest.

L1 and L2 regularization both have shortcomings for the decomposition problem posed here. These shortcomings will be demonstrated empirically in the results. To overcome these, we use elastic-net regularization to perform the ADMIRE decomposition [35]. Elastic-net regularization solves the following optimization problem,

$$\hat{\beta} = \arg\min_{\beta}(\|y - X\beta\|^2 + \lambda(\alpha\|\beta\|_1 + (1-\alpha)\|\beta\|_2^2/2)), \tag{15}$$

where $\|\beta\|_1 = \sum_{n=0}^{N} |\beta_n|$ is the L1 term, $\|\beta\|_2 = \sqrt{\sum_{n=0}^{N} |\beta_n|^2}$ is the L2 term, α is between 0 and 1 and determines the relative weight between L1 and L2, and λ is the total regularization parameter. Elastic-net regularization is attractive because it allows for correlated model predictors to be present simultaneously due to L2, but it also allows for non-zero model predictors due to the L1 term. These regularization schemes tends to introduce related sets of correlated model components as a cluster, which has been referred to as group selection. Elastic-net regularization becomes an L1 problem if $\alpha = 1$ and L2 if $\alpha = 0$. The elastic-net and the limiting L1 and L2 regularization problems are solved using the efficient software package glmnet [36].

In order to appropriately compare models with different α and λ values it is useful to know the degrees of freedom for a given model. The general degrees of freedom for an elastic net regularized regression solution is

$$\begin{aligned} df(\lambda) &= Tr[X_{\mathcal{A}}(X_{\mathcal{A}}^T X_{\mathcal{A}} + \lambda I)^{-1} X_{\mathcal{A}}^T] \\ &= \sum_{n=0}^{P-1} \frac{d_n^2}{d_n^2 + \lambda}, \end{aligned} \tag{16}$$

where $X_{\mathcal{A}}$ is a reduced model composed of only predictors with non-zero coefficient estimates and d_n values are singular values of the reduced model [37]. The singular value decomposition was performed iteratively using an efficient memory approach to accommodate the potential for large model matrices [38].

D. Signal Reconstruction

Once the signal has been spatially decomposed using the model, the final step in ADMIRE is to reconstruct a clean signal. This is accomplished by identifying model predictors within the region of interest specified by (14), which we denote as $X_{\mathcal{B}}$. The signal from the region of interest is reconstructed as

$$y_{ROI} = X_{\mathcal{B}} \hat{\beta}_{\mathcal{B}}. \tag{17}$$

The clutter suppressed signals are converted back to time-domain channel data using an inverse short-time Fourier transform (ISTFT).

E. Short-Time Fourier Transform

The STFT used here is implemented as

$$S_i(mT, \omega_p) = \sum_{l=-\infty}^{\infty} s(l) w_{FT}(mT - l) e^{-j\omega_p l}, \tag{18}$$

where T denotes the time sampling period of the STFT, $w_{FT}(l)$ is the sliding window that selects the short-time segments, and ω_p are the discrete frequencies, typically distributed as $2\pi k/N$ for $k = [0, ...N-1]$. To make the connection back to the model clear, $S_i(mT, \omega_p)$ would be the STFT for a single channel of the aperture, where each channel is indexed by i, and this index corresponds to x in $p_s(x; t, \omega)$.

An ISTFT is used to reconstruct the time-domain signal after the model decomposition and aperture domain signal reconstruction. The inverse transformation back into the original domain is accomplished using the least-squares ISTFT described by Yang [39], which is

$$s_i(n) = \frac{w_{FT}(mT - l) \sum_{\omega_p=-\infty}^{\infty} S_i(mT, \omega_p) e^{j\omega_p l}}{\sum_{l=-\infty}^{\infty} w_{FT}(mT - l)^2}. \tag{19}$$

F. Computational Complexity

Signal decomposition using elastic net regularization has a computational order of $\mathcal{O}(m^3 + sm^2)$ where s is the number of predictors in the model matrix, X, and m is the number of steps in the L1 portion of the model-fit. [35]. (The computational complexity matches the complexity for a single ordinary least squares fit.)

G. Multipath simulations for regularization tuning

The ADMIRE model fit described by (15) requires two different regularization parameters to be empirically determined, α and λ. These parameters are the total regularization weight (λ) and the balance between L1 and L2 (α). The tuning problem here is slightly different from conventional tuning problems because for imaging applications we are most interested in the error from only part of our signal, which is the signal returning from the region of interest. That is, after solving the elastic-net regularized optimization problem in (15), we obtain a set of non-zero predictors $X_{\mathcal{A}}$, and of these predictors, some additionally reduced set $X_{\mathcal{B}}$ will represent scatterers within the region of interest that will form the reconstructed signal. For imaging, the primary goal is to minimize the error of the signal of interest while maximizing suppression of energy originating outside of the acceptance zone. The error of the signal of interest is described as,

$$err_{ROI} = ||y_{ROI} - X_{\mathcal{B}} \hat{\beta}_{\mathcal{B}}||^2, \tag{20}$$

where y_{ROI} is the wavefront formed by scattering only from the region of interest, and $\beta_{\mathcal{B}}$ are the coefficients corresponding to the predictors within the ROI. In order to estimate the reconstruction error, err_{ROI}, it is necessary to know the true wavefront of interest. The true wavefront is not knowable when using *in vivo* data, and using fully non-linear simulations can also make knowing the true signal of interest difficult. Therefore, for model validation, basic image evaluation and regularization tuning we propose a pseudo-nonlinear approach to simulating multipath scattering induced signal corruption using the linear simulation package Field II [40], [41]. Field II already naturally simulates off-axis scattering and scattering from a specified region of interest, which means that once we introduce our extension, Field II can simulate all the degradation mechanisms of interest here.

To add our multipath Field II extension, we simulate multipath scattering by simulating channel data for scatterers arriving from a particular depth without any receive beamforming. We then shift the data to a later time by zero-padding and interpolating the data in the time-domain to a specific time of interest. Once the multipath signals are simulated and delayed they are added to the signal of interest. The channel data from multipath scattering can be scaled to simulate various levels of clutter.

This approach allows for simulations with both off-axis and multipath clutter sources that are known exactly. For example, clutter from many different regions can be simulated, and then the amplitude of all of these clutter signals can be normalized relative to the signal of interest to create clutter with known power. Additionally, clutter from discrete scatterers can be simulated, or clutter from diffuse scatterer sites can be used to create a more complex and possibly more realistic clutter signal. Currently, each lateral line location is treated separately, which means that the lateral correlation does not mimic the expected behavior. In principle this can be accounted for, but we do not address this at this point because our algorithm is not affected by lateral correlation.

The motivation for this pseudo-nonlinear simulation approach was to easily calculate err_{ROI}, but the simulation scheme also allows for a simple contrast metric and provides more insight into regularization tuning. The contrast metric is calculated from clutter data with and without a signal of interest. This correlates to estimating the contrast of an anechoic cyst. The signal that contains both clutter and a signal of interest represents the background feature, and the signal with only cluter represents

TABLE I: Field II Simulation Parameters

Parameter	Value
Center Frequency (f_c)	3 MHz
Bandwidth	60%
Lateral Pitch	0.257 mm
Elevation Width	2 mm
Samp. Freq. (Simulation)	640 MHz
Samp. Freq. (Downsampled)	40 MHz
Transmit Focal Depth	3 cm
Transmit f-number	1.8
Receive f-number	2
Lesion Radius	2 mm
Lesion Center Depth	3 cm

TABLE II: Decomposition Parameters

Parameter	Value
STFT Window Length	$\frac{8\log(2)}{2\pi BW f_0}$
STFT Padded Window Length	2 $\times$ Window Length
STFT Window Type	Rectangular
STFT Window Overlap	90%
Decomposed Bandwidth	120%
c_l	6
c_a	2
γ	*variable*
α	*variable*
λ	*variable*
Sampling Grid	*variable*

an anechoic lesion feature. The metric is calculated using

$$C_{reg} = 20log_{10}\frac{\mathrm{w}^H(X_{\mathcal{B}}\hat{\beta}_{\mathcal{B}})_{\text{clutter only simulation}}}{\mathrm{w}^H(X_{\mathcal{B}}\hat{\beta}_{\mathcal{B}})_{\text{signal and clutter simulation}}} \tag{21}$$

where w is a beamforming vector that corrects for intentional modulation before summing and H is the complex transpose. This metric provides insight into how well the signal of interest's power is preserved compared to how well the power of the clutter is suppressed.

H. Field II Contrast Simulations

In addition to using Field II to help tune the regularization parameters, Field II is also used to evaluate ADMIRE's performance on linear simulations of contrast phantoms. The motivation is to determine how well the decomposition algorithm preserves contrast and contrast-to-noise ratio (CNR) in uncluttered data. This is important because in our previous model and decomposition scheme CNR was reduced in about half of the data; however, because most of the previous analysis was performed on *in vivo* data, the exact cause of the CNR decrease was impossible to determine because decreases in CNR could be due to increased structure like blood vessels exposed in the background region. To address this, a number of Field II simulation experiments were conducted using the parameters in Table I. Contrast phantoms were simulated with lesion contrasts of totally anechoic, -20 dB, -10 dB, -5 dB, 5 dB, 10 dB and 20 dB. Each contrast level was simulated with twelve independent speckle realizations. For each data set we measured the contrast as,

$$C = -20log_{10}\left(\frac{\mu_{lesion}}{\mu_{background}}\right), \tag{22}$$

the CNR as

$$CNR = 20log_{10}\left(\frac{|\mu_{background} - \mu_{lesion}|}{\sqrt{\sigma^2_{background} + \sigma^2_{lesion}}}\right), \tag{23}$$

and the speckle SNR as

$$SNR_{speckle} = \frac{\mu_{background}}{\sigma_{background}}, \tag{24}$$

where μ and σ^2 denote the indicated mean and variance , respectively, of the enveloped but uncompressed regions of the image data.

Field II was also used to simulate cluttered contrast phantoms. In this case anechoic lesions were simulated with signal to clutter ratios of 0 dB, 10 dB and 20 dB. The clutter that was added to the anechoic lesion simulations was made using the multipath scattering approach described earlier. Approximately 8 diffuse clutter sites were added to the signal every 0.25 mm. The clutter sites could originate from anywhere shallow to the region where they would be added to the linear simulation and up to 1 cm on either side of the transmit beam's axis. Each diffuse clutter site contained 25 scatterers.

I. In Vivo Examples

We evaluated ADMIRE on three *[in vivo]* data sets acquired with a Siemens S2000 and 4C-1 curvilinear array (Siemens Healthcare, Ultrasound Business Unit, Mountain View, CA). Two of the data cases were acquired at 4 MHz, and the third was a harmonic pulse inversion sequence with a 1.8 MHz transmit frequency and a 3.6 MHz center frequency on receive. ADMIRE was applied to the data as described. The model sampling parameters for the region of interest were $0.167res_{lat}$, $0.668res_{axl}$, and 0.0485λ for the lateral, axial and phase dimensions, respectively. Outside the region of interest the sampling was $3.35res_{lat}$, $3.35res_{axl}$ and 0.2423λ for the lateral axial and phase dimensions, respectively. For comparison the data sets were beamformed with and without hamming apodization on receive. Apodization was applied after ADMIRE.

III. Results

A. Model Error and Clutter Correlation Patterns

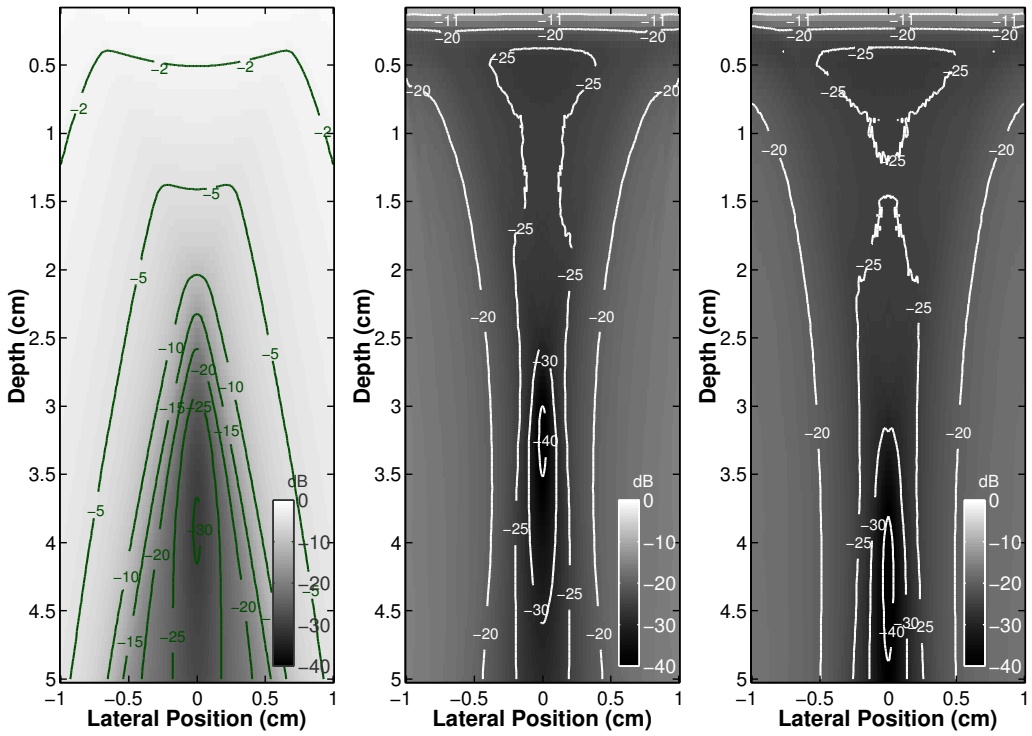

(a) Old Model (b) New Model γ=0 (c) New Model γ=0.5

Fig. 4: Model error power is shown for the old model (a), the proposed model without additional modulation (b), and the new model with an additional modulation corresponding to $\gamma = 0.5$ (c). The new model has distinctly lower model error compared to the old model. The new model has low error for both cases, but the case of the intentional receive modulation has slightly lower error.

Model errors are shown in Fig. 4. The figure compares the model error for our previous model and two realizations of the current model. The region of interest is at 5 cm for the results shown in the figure. The results show that the error for the new model is similar regardless of the modulation, but the modulation does allow the region of interest to be decomposed with the lowest error predictors, and it increases the size of the region with error less than -20 dB. The model error for all the models becomes high in the very near-field, which may be related to the performance of Field II in the near-field.

B. Example of a Simulated Cluttered Wavefront

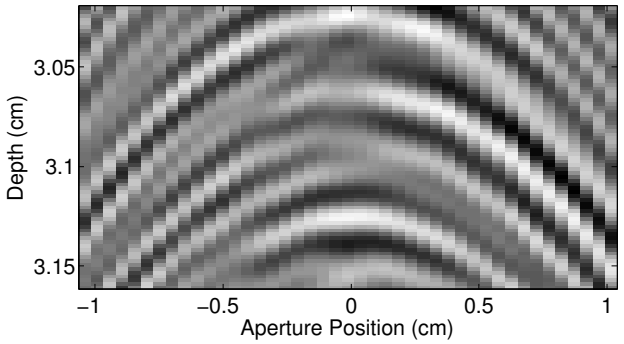

(a) Normal Field II

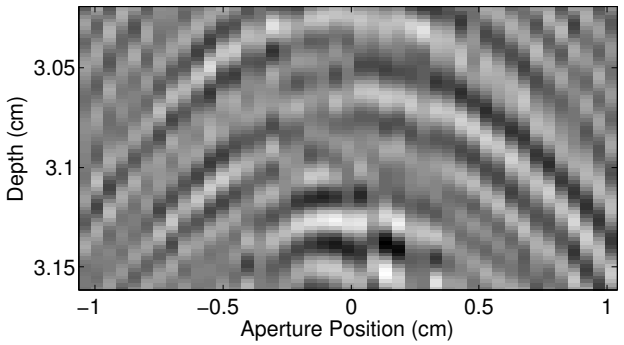

(b) Field II with Simulated Clutter

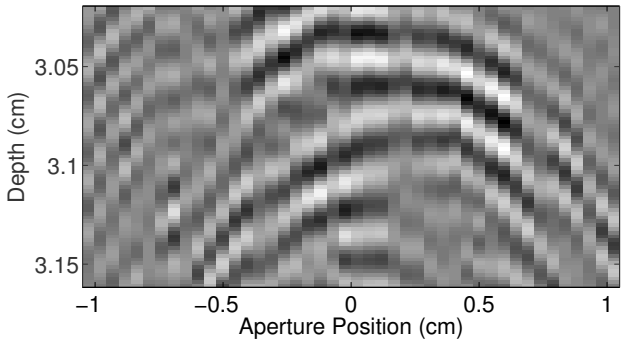

(c) *In Vivo* Data

Fig. 5: An example of the multipath Field II simulations is shown. In (a) a normal Field II simulation is shown. In (b) the same Field II simulation corrupted by Field II simulated multipath scattering is shown. In (c) an *in vivo* example featuring several distinct wavefronts is shown. The Field II simulation with simulated multipath and off-axis clutter features some similarities to the *in vivo* data that are not present in the usual Field II simulation. For example, in the *in vivo* and cluttered simulation there are apparent sharp discontinuities in the wavefront that are not apparent in the first Field II simulation.

We show an example of simulated cluttered data using the approach described in the methods in Fig. 5. The figure shows an uncluttered Field II simulation and the same Field II simulation cluttered with simulated multipath and off-axis scattering. The cluttered simulation contains qualitative features similar to the *in vivo* data, which includes sharp discontinuities across the aperture and apparent suppression of the wavefront in some regions. From visual inspection of the *in vivo* data there is likely also sound-speed variation (i.e. phase-aberration) errors, which is not currently included in the simulation approach introduced here.

C. Regularization Parameters

The results of varying α and λ from (15) are shown in Fig. 6. These results demonstrate several important ideas about the ADMIRE model-fit, and the advantages of incorporating an elastic-net scheme instead of solely L1 ($\alpha = 1$) or L2 ($\alpha = 0$) regularization. Figs. 6a and 6c show the decrease in the full signal error as a function of increasing degrees of freedom. (In this case plotting the independent axis using degrees of freedom instead of lambda more readily enables comparison between

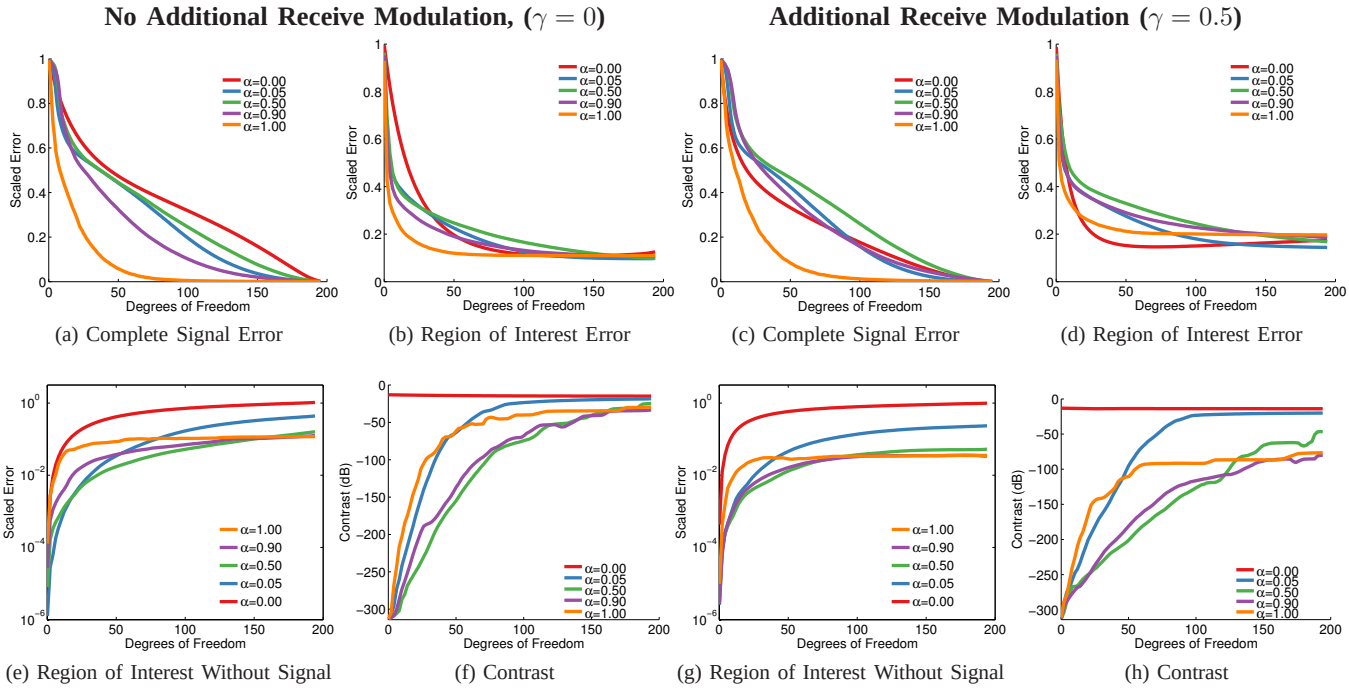

(a) Complete Signal Error (b) Region of Interest Error (c) Complete Signal Error (d) Region of Interest Error

(e) Region of Interest Without Signal (f) Contrast (g) Region of Interest Without Signal (h) Contrast

Fig. 6: Several different errors are shown as a function of degrees of freedom for several values of α between L1 (lasso regression) and L2 (ridge regression) regularized model-fits. Figs. 6a and 6c imply that L1 is the best scheme for minimizing the error of the complete aperture domain signal; however, Figs. 6b and 6d demonstrate that L2 produces the lowest error for the wavefront returning from the region of interest. These results are mitigated by the results in Figs. 6e, 6g, 6f and 6h, which demonstrate that an α value between 0 and 1 performs better at suppressing signals outside the region of interest and adequately reconstructing the wavefront originating from the region of interest.

different values of α, which are each optimized with different λ values.) Displaying the data against degrees of freedom initially suggests that L1 produces the best fit with the smallest error for small degrees of freedom. This result is usually desirable; however, in this case L1 does not always produce the lowest error of the wavefront of interest, which is shown in Figs. 6b and 6d. We also show that L1 does not produce the best improvement in contrast, which is shown in Figs. 6f and 6h. The end result is that while L1 results in the best decomposition of the cluttered signal, L1 does not lead to the best decluttered image.

For the task of reconstructing the wavefront of interest L2 can achieve the lowest mean square error with the fewest degrees of freedom. However, while L2 reconstructs the signal shape well; L2 by itself fails to effectively reject sources of clutter originating outside the region of interest as demonstrated in Figs. 6e, 6g, 6f and 6h.

Figs. 6e, 6g show the amount of energy in the signal of interest when the true signal is composed only of clutter sources (lower is better). This represents the scenario of a truly anechoic cyst. This is further emphasized in Figs. 6f and 6h showing the image contrast proxy, (21).

D. Image Quality

Example lesions of the uncluttered linear contrast simulations are shown in Fig. 7. These results show good qualitative agreement without clutter. The summary statistics for the contrast simulations are displayed in Fig. 8. These results compare normal B-Mode versus B-Mode images formed from several different sets of regularization parameters. The contrast simulation results are summarized using contrast, CNR and speckle SNR. The primary result is that ADMIRE preserves normal B-Mode imaging metrics when clutter is not present, and in a few cases ADMIRE does better, such as with the anechoic contrast simulation. This is important because it demonstrates that ADMIRE does not degrade or otherwise corrupt high-quality B-Mode data.

Example lesions of cluttered anechoic contrast simulations are shown in Fig. 9. These results provide an example of how the Field II multipath clutter image degradation looks for various signal to clutter levels. The summary statistics in Fig. 10 demonstrate that the ADMIRE images largely have better image metrics. The change in CNR is modest, but this small improvement in CNR may be correlated to the relatively high variance inside the lesion even after decluttering.

In order to demonstrate that the simulation results translate to *in vivo* data three examples are shown in Fig. 11 with contrast and CNR metrics compiled in Table III. Results are shown for several sets of regularization parameters. For each set of parameters the contrast is clearly better compared to the original data, but in some cases the CNR decreases. However, based

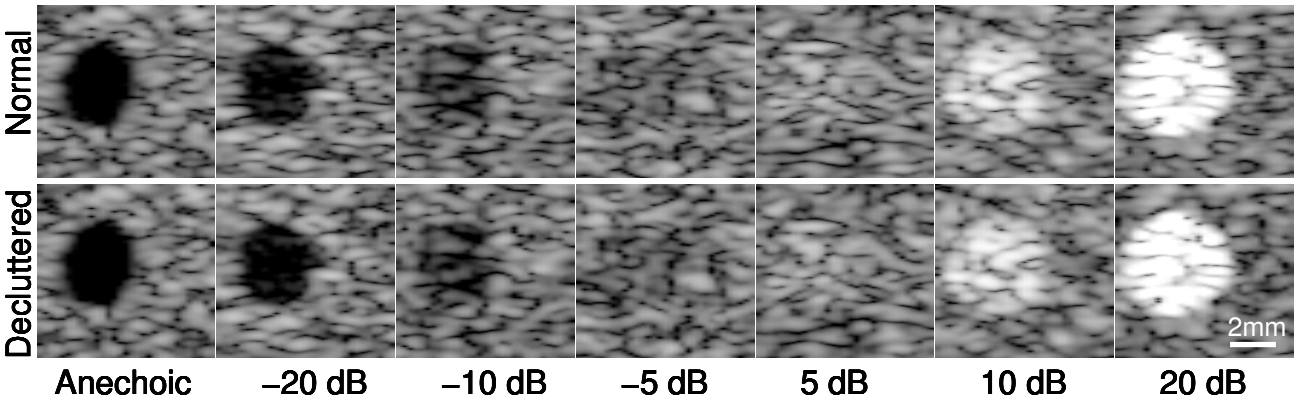

Fig. 7: 4 mm lesions are visualized using a 3 MHz F/2 imaging system. The contrast of the simulated phantoms goes from completely anechoic to +20 dB. For all cases there is little change between the decluttered and normal B-Mode data. The full summary of all the simulations is shown in Fig. 8, but the result is that the decluttering algorithm does not produce images with worse image metrics in the absence of clutter.

TABLE III: *In vivo* Image Metrics

Parameters	Cont.(dB)		CNR(dB)	
	rect.	Hamm.	rect.	Hamm.
Case #1 (Fundamental)				
Normal B-Mode	12.4	13.1	0.76	0.49
$\alpha = 1$, $\gamma = 0$	17.6	19.9	0.17	0.30
$\alpha = 0.9$, $\gamma = 0$	20.9	23.6	0.50	0.61
$\alpha = 0.9$, $\gamma = 0.5$	37.2	41.2	1.38	0.64
Case #2 (Fundamental)				
Normal B-Mode	13.9	14.3	1.28	1.70
$\alpha = 1$, $\gamma = 0$	17.8	18.3	1.40	1.98
$\alpha = 0.9$, $\gamma = 0$	18.5	19.1	1.48	2.10
$\alpha = 0.9$, $\gamma = 0.5$	24.7	25.1	2.06	2.30
Case #3 (Harmonic)				
Normal B-Mode	12.2	12.6	-1.15	-0.95
$\alpha = 1$, $\gamma = 0$	19.0	19.2	-0.47	-0.42
$\alpha = 0.9$, $\gamma = 0$	19.8	20.0	-0.35	-0.29
$\alpha = 0.9$, $\gamma = 0.5$	24.0	24.7	0.05	0.10

on the previous CNR results from Field II simulations and visual inspection of the *in vivo* example cases shown in Fig. 11 it is reasonable to attribute the decrease in CNR to additional structure introduced in the background region used to calculate the image metrics. Similar levels of improvement are encountered when ADMIRE is applied to fundamental or harmonic data. We also report the full run time for each of the *in vivo* cases using $\alpha = 0.9$ and $\gamma = 0.5$ and operating on a single core of an Intel Core i7-4790 3.60GHz processor (Intel Corporation, Santa Clara, CA). The total serial run times for the fundamental cases were 46,932s and 46,540s. The harmonic run time was 27,542.

IV. Discussion

We have presented a new model and decomposition approach for the ultrasound clutter problem, which we refer to as ADMIRE. ADMIRE solves many of the open questions from our previous method. These include preservation of image-quality and decomposition issues. One significant question from before was how many model components to include in the final decomposition. This is now a function of the regularization constraints and can be tuned to maximize image quality. It should be noted that some of the image quality improvements are related to better STFT and ISTFT parameters compared to those coupled to our previous algorithm, and therefore even the old model and decomposition scheme perform better than in the original implementation [30].

In order to support ADMIRE a pseudo non-linear modification to Field II was introduced. We presented a qualitative demonstration of this approach for generating realistic clutter, but the ultimate goal was to develop a useful tool for tuning the regularization parameters. To this end, the unique application of Field II to generate multipath scattering was successful at generating regularization parameters that translated successfully to both fundamental and harmonic *in vivo* data.

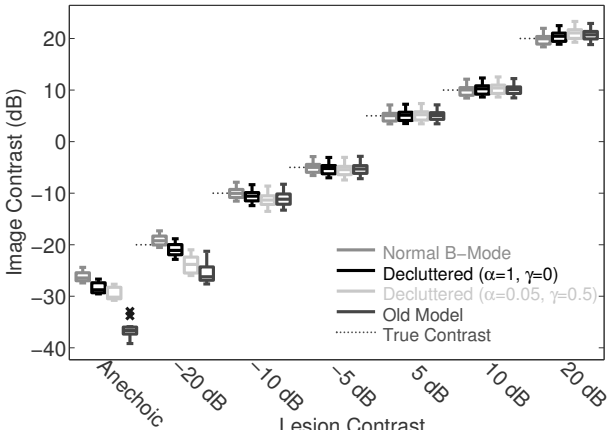

(a) Contrast

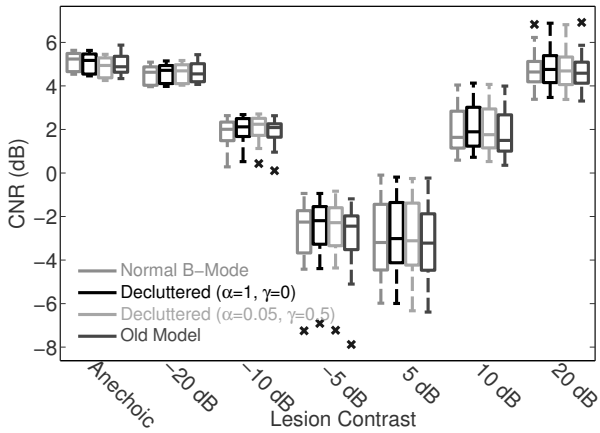

(b) Contrast-to-Noise Ratio

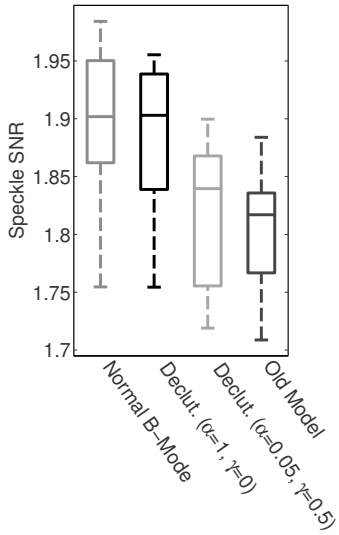

(c) Speckle SNR

Fig. 8: The results of 12 speckle realizations are shown as boxplots for several levels of lesion contrast and CNR. Results are also shown for speckle SNR. Results are shown for normal B-Mode, and the new and old models. In these results the shortcomings of the old model are clearly evident in the CNR and speckle SNR data, but in contrast the new model does not have worse CNR or speckle SNR than normal B-Mode imaging. In some instances the CNR may be slightly better compared to B-Mode imaging.

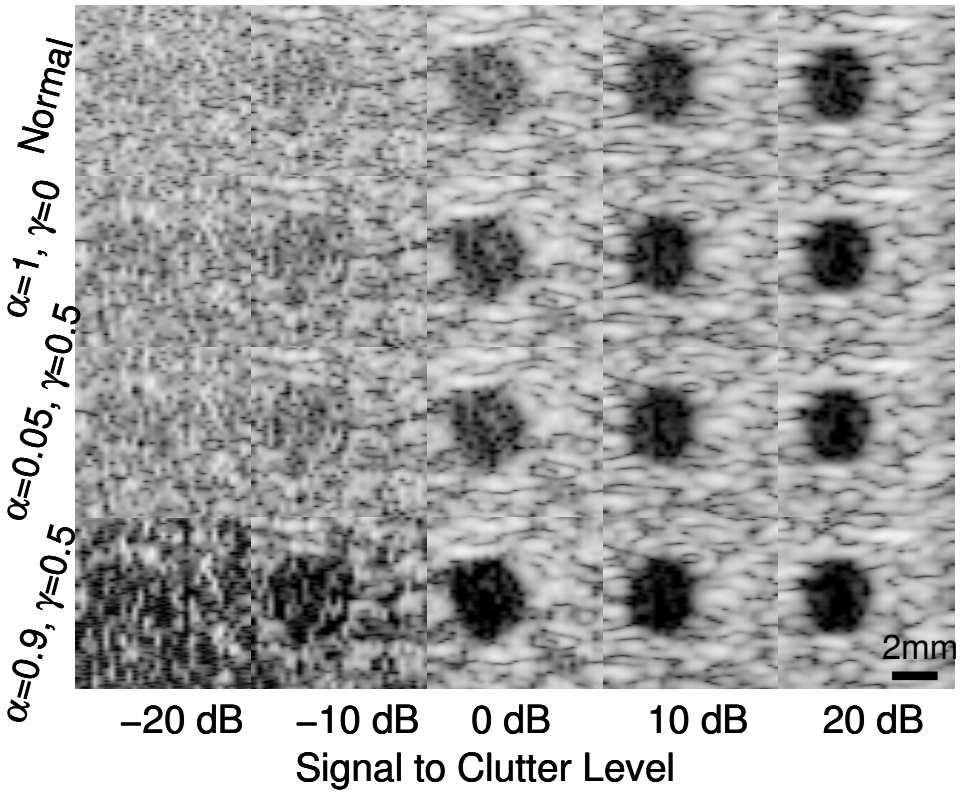

Fig. 9: 4 mm lesions are visualized using a 3MHz F/2 imaging system. The contrast of the simulated phantoms goes from completely anechoic to +20 dB. For all cases there is little change between the decluttered and normal B-Mode data. The full summary of all the simulations is shown in Fig. 10, but the result is that ADMIRE does not produce images with worse image metrics in the absence of clutter.

In our implementation of the model we assumed that a Gaussian envelope was a reasonable representation of the pulse shape. This assumption was not rigorously tested here, but qualitative inspection of the *in vivo* data does not reveal gross changes in the speckle pattern or the resolution between normal and decluttered B-Mode images. Also as mentioned previously our algorithm is not dependent on the Gaussian pulse approximation, and if necessary future algorithms can implement more sophisticated approaches to better account for the pulse shape.

ADMIRE's biggest drawback is run time. The reported run times for the example cases are a few hours per frame, which is the serial run time for a Matlab implementation. The algorithm itself is easily parallelized, but even with a massively parallel graphical processing unit (GPU) based implementation this would likely still require several seconds per frame. Moving forward it will be important to consider computational or algorithmic modifications that can reduce processing time without sacrificing the demonstrated improvements.

While the improvements realized in the *in vivo* examples shown in Figs. 11 and 12 are compelling, the reduced clutter could lead viewers to inappropriately put diagnostic emphasis on clutter that is not eliminated. It is important to realize that the current implementation is only designed to act on reverberation and off-axis scattering distributed along the axial and lateral dimensions. Image degradation from other sources like diffraction limitations, phase aberration or clutter from out of the imaging plane are not addressed here. These mechanisms of degradation could be integrated into ADMIRE in the future.

Finally, it is important to mention that although we are decomposing the received signal into a specific set of scatterers, there are multiple distributions of scatterers that can recreate any given wavefront. The specific scatterers that end up in the final model-fit are a function of the model space sampling and the choice of regularization parameters. Based on this, we do not assume that there is any connection between the non-zero coefficients from the model fit and the actual scatterers in the imaged media. We do assume that the collection of scatterers within a given region considered as a whole are representative of the actual wavefront returning from a given region of tissue.

V. Conclusions

The problem of acoustic clutter is unresolved, and is still responsible for failed exams in many patients. To resolve this issue we proposed a new model-based approach, ADMIRE. The approach declutters and preserves the RF-channel data, which means it should be able to function in conjunction with other classic ultrasound algorithms. Our results show that ADMIRE preserves B-mode image quality and acts as an all-pass filter when clutter levels are minimal; however, as clutter levels increase

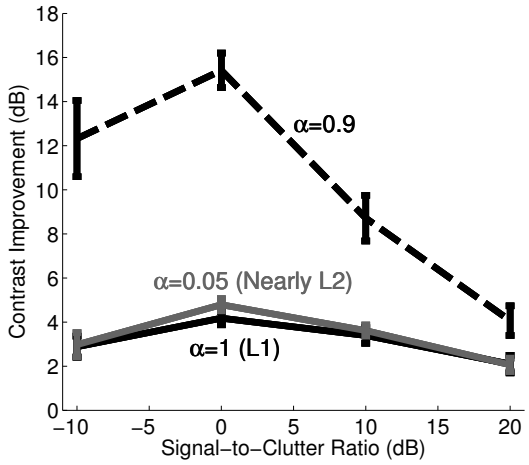

(a) Contrast

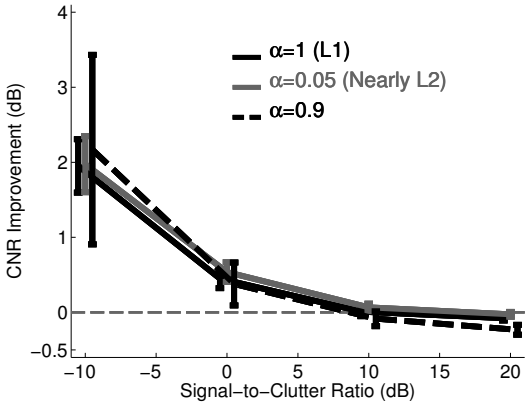

(b) Contrast-to-Noise Ratio

Fig. 10: The results of cluttered anechoic lesion simulations are shown as boxplots for several levels of signal-to-clutter ratio. Results are shown for several different sets of regularization parameters. The results mostly show that the ADMIRE images are better, but with very high or very low levels of signal-to-clutter ratio the improvement is not substantial. The largest improvement are seen from the images formed using $\alpha = 0.9$ and $\gamma = 0.5$

ADMIRE effectively suppresses clutter energy, restoring image quality. Finally, it is worth noting that the final output is still a B-Mode image, which is consistent with the training of current healthcare workers.

ACKNOWLEDGMENT

The authors would like to thank Ned Danieley and Mark Palmeri for computer assistance, and the staff of the Vanderbilt University ACCRE computing resource. We would also like to thank the reviewers for their helpful comments and Jeremy Dahl and Marko Jakovljevic for insightful suggestions. This work was supported by NIH grant 1S10RR026828.

REFERENCES

[1] R. Smith-Bindman, D. L. Miglioretti, E. Johnson, C. Lee, H. S. Feigelson, M. Flynn, R. T. Greenlee, R. L. Kruger, M. C. Hornbrook, D. Roblin, L. I. Solberg, N. Vanneman, S. Weinmann, and A. Williams, "Use of Diagnostic Imaging Studies and Associated Radiation Exposure for Patients Enrolled in Large Integrated Health Care Systems, 1996-2010," *Journal of the Americal Medical Association*, vol. 307, no. 22, pp. 2400–2409, 2012.

[2] B. C. Flynn, J. Spellman, C. Bodian, and V. K. Moitra, "Inadequate visualization and reporting of ventricular function from transthoracic echocardiography after cardiac surgery." *Journal of cardiothoracic and vascular anesthesia*, vol. 24, no. 2, pp. 280–4, Apr. 2010.

[3] P. A. Heidenreich, R. F. Stainback, R. F. Redberg, N. B. Schiller, N. H. Cohen, and E. Foster, "Transesophageal echocardiography predicts mortality in critically ill patients with unexplained hypotension." *Journal of the American College of Cardiology*, vol. 26, no. 1, pp. 152–8, Jul. 1995.

[4] I. Hendler, S. C. Blackwell, E. Bujold, M. C. Treadwell, P. Mittal, R. J. Sokol, and Y. Sorokin, "Suboptimal second-trimester ultrasonographic visualization of the fetal heart in obese women: should we repeat the examination?" *Journal of ultrasound in medicine : official journal of the American Institute of Ultrasound in Medicine*, vol. 24, no. 9, pp. 1205–9; quiz 1210–1, Sep 2005.

[5] F. R. Khoury, H. M. Ehrenberg, and B. M. Mercer, "The impact of maternal obesity on satisfactory detailed anatomic ultrasound image acquisition." *The journal of maternal-fetal & neonatal medicine : the official journal of the European Association of Perinatal Medicine, the Federation of Asia and Oceania Perinatal Societies, the International Society of Perinatal Obstetricians*, vol. 22, no. 4, pp. 337–41, Apr. 2009.

[6] M. Kurt, K. A. Shaikh, L. Peterson, K. M. Kurrelmeyer, G. Shah, S. F. Nagueh, R. Fromm, M. A. Quinones, and W. A. Zoghbi, "Impact of contrast echocardiography on evaluation of ventricular function and clinical management in a large prospective cohort." *Journal of the American College of Cardiology*, vol. 53, no. 9, pp. 802–10, Mar. 2009.

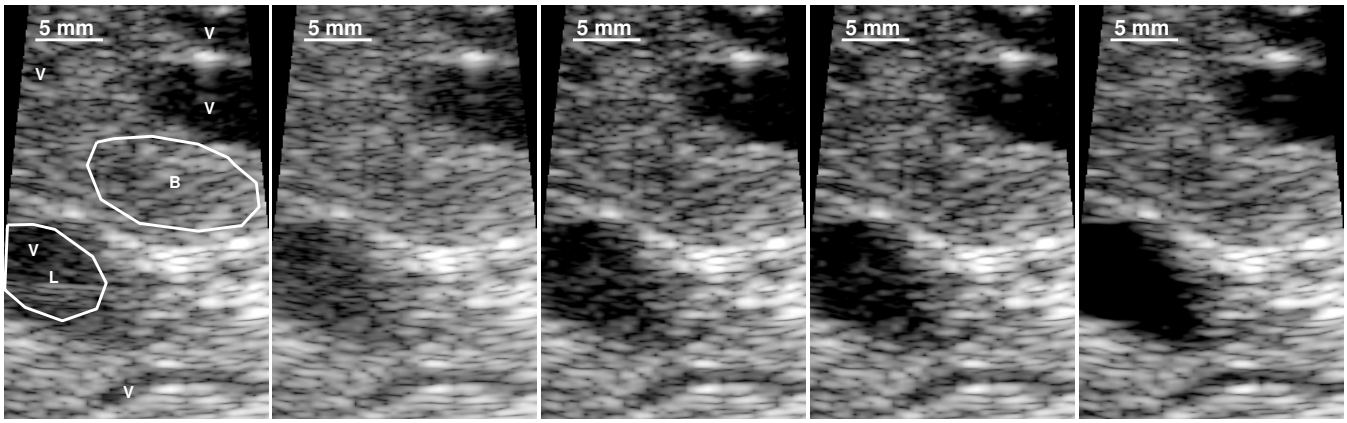

(a) Mask Regions (b) Normal B-Mode (c) $\alpha = 1$, $\gamma = 0$ (d) $\alpha = 0.9$, $\gamma = 0$ (e) $\alpha = 0.9$, $\gamma = 0.5$

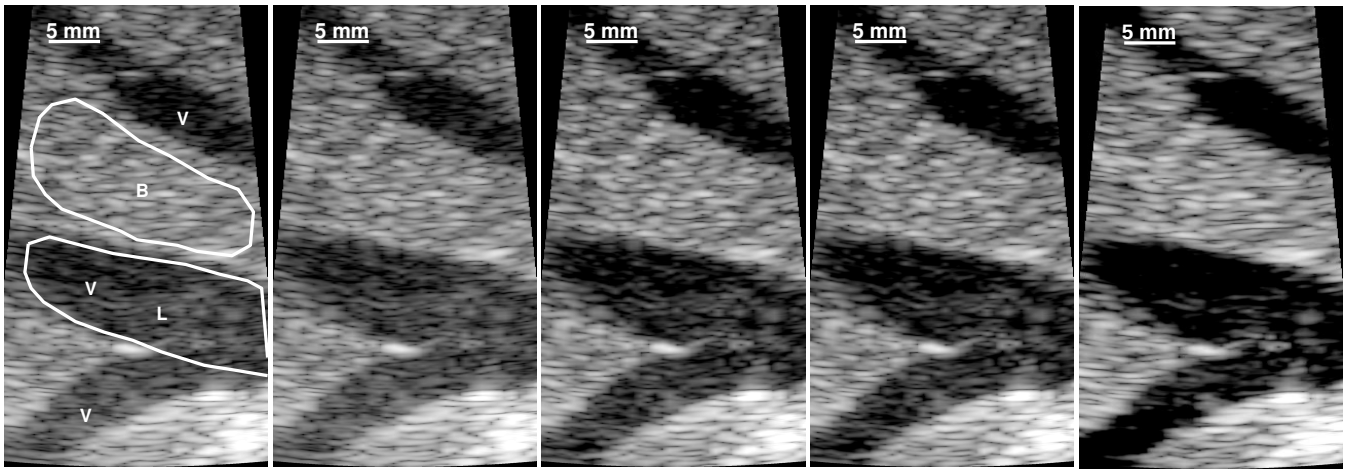

(f) Mask Regions (g) Normal B-Mode (h) $\alpha = 1$, $\gamma = 0$ (i) $\alpha = 0.9$, $\gamma = 0$ (j) $\alpha = 0.9$, $\gamma = 0.5$

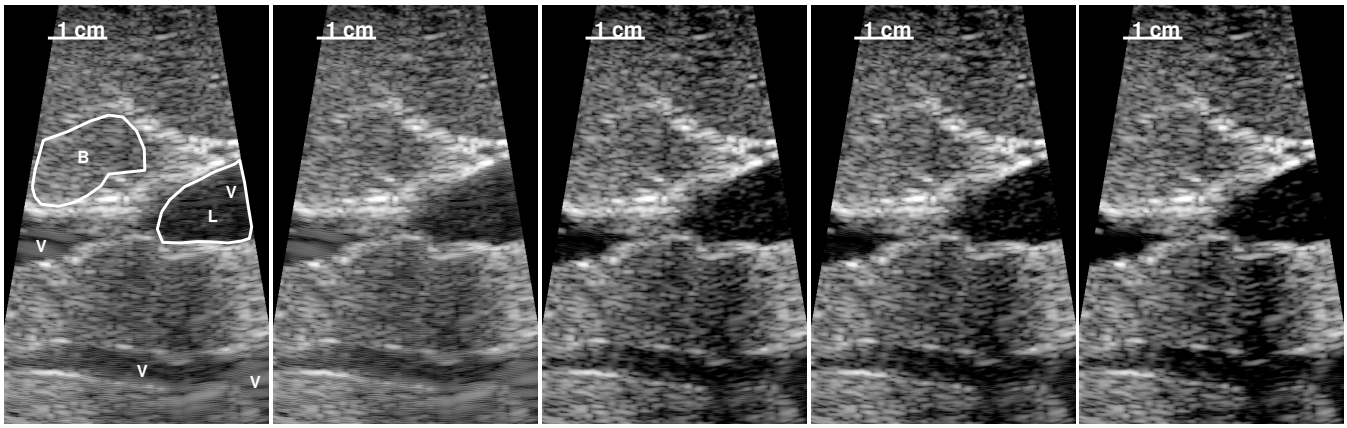

(k) Mask Regions (l) Harmonic B-Mode (m) $\alpha = 1$, $\gamma = 0$ (n) $\alpha = 0.9$, $\gamma = 0$ (o) $\alpha = 0.9$, $\gamma = 0.5$

Fig. 11: Three *in vivo* examples are shown to demonstrate that ADMIRE translates to both fundamental and harmonic clinical data. The results are qualitatively promising, and quantitative image metrics presented in Table III support the qualitative improvements. Hypoechoic regions of the image presumed to be vessels are indicated with 'V', and the regions used to calculate image metrics are outlined and denoted with an 'L' or 'B' indicating lesion or background, respectively. In both cases image improvements in the large structures are clear. In the first example, there is evidence that previously unvisualizable vessels (upper left corner) become visible after decomposition.

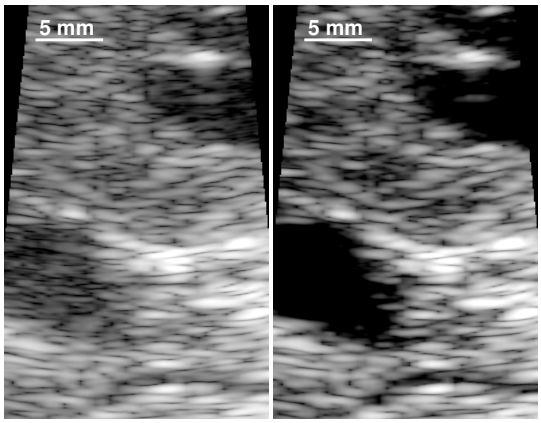

(a) Normal B-Mode (b) $\alpha = 0.9$, $\gamma = 0.5$

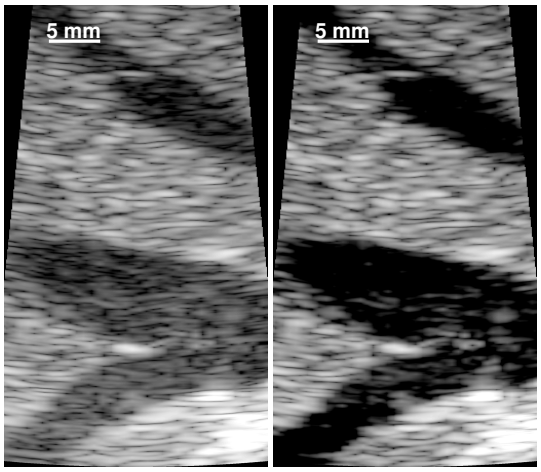

(c) Normal B-Mode (d) $\alpha = 0.9$, $\gamma = 0.5$

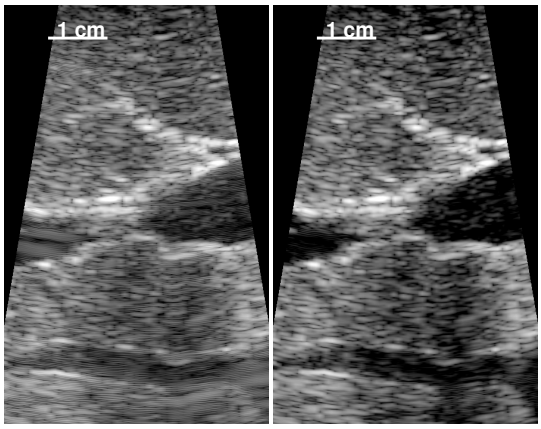

(e) Harmonic B-Mode (f) $\alpha = 0.9$, $\gamma = 0.5$

Fig. 12: The effect of applying a hamming apodization window on receive is shown on the fundamental and harmonic B-Mode images and the corresponding data after ADMIRE with the $\alpha = 0.9$ and $\gamma = 0.5$ case. The *in vivo* examples show that apodization only results in modest improvements compared to ADMIRE. The matched contrast and CNR results are shown in Table III

[7] G. F. Pinton, G. E. Trahey, and J. J. Dahl, "Erratum: Sources of image degradation in fundamental and harmonic ultrasound imaging: a nonlinear, full-wave, simulation study." *IEEE transactions on ultrasonics, ferroelectrics, and frequency control*, vol. 58, no. 6, pp. 1272–83, Jun. 2011.

[8] S. W. Flax and M. O'Donnell, "Phase-aberration correction using signals from point reflectors and diffuse scatterers: basic principles." *IEEE transactions on ultrasonics, ferroelectrics, and frequency control*, vol. 35, no. 6, pp. 758–67, Jan. 1988.

[9] D. L. Liu and R. C. Waag, "Correction of ultrasonic wavefront distortion using backpropagation and a reference waveform method for time-shift compensation," *The Journal of the Acoustical Society of America*, vol. 96, no. 2 Pt 1, pp. 649–60, Aug. 1994.

[10] S. Krishnan, P.-c. Li, and M. O'Donnell, "Adaptive Compensation of Phase and Magnitude Aberrations," *IEEE Trans. Ultrason. Ferroelect. Freq. Contr.*, vol. 43, no. 1, pp. 44–55, 1996.

[11] C. H. Seo and J. T. Yen, "Sidelobe suppression in ultrasound imaging using dual apodization with cross-correlation." *IEEE transactions on ultrasonics, ferroelectrics, and frequency control*, vol. 55, no. 10, pp. 2198–210, Oct. 2008.

[12] D. A. Guenther and W. F. Walker, "Robust finite impulse response beamforming applied to medical ultrasound." *IEEE transactions on ultrasonics, ferroelectrics, and frequency control*, vol. 56, no. 6, pp. 1168–88, Jun. 2009.

[13] Z. Wang, J. Li, and R. Wu, "Time-delay- and time-reversal-based robust Capon beamformers for ultrasound imaging." *IEEE transactions on medical imaging*, vol. 24, no. 10, pp. 1308–22, Oct. 2005.

[14] I. K. Holfort, F. Gran, and J. r. A. Jensen, "Broadband minimum variance beamforming for ultrasound imaging." *IEEE transactions on ultrasonics, ferroelectrics, and frequency control*, vol. 56, no. 2, pp. 314–25, Feb. 2009.

[15] J.-F. Synnevag, A. Austeng, and S. Holm, "Adaptive beamforming applied to medical ultrasound imaging," *Ultrasonics, Ferroelectrics and Frequency Control, IEEE Transactions on*, vol. 54, no. 8, pp. 1606–1613, August 2007.

[16] H. Becher, K. Tiemann, T. Schlosser, C. Pohl, N. C. Nanda, M. a. Averkiou, J. Powers, and B. Lüderitz, "Improvement in Endocardial Border Delineation Using Tissue Harmonic Imaging." *Echocardiography*, vol. 15, no. 5, pp. 511–518, Jul. 1998.

[17] K. Spencer, J. Bednarz, P. Rafter, C. Korcarz, and R. Lang, "Use of harmonic imaging without echocardiographic contrast to improve two-dimensional image quality," *The American Journal of Cardiology*, vol. 82, no. 6, pp. 794–799, Sep. 1998.

[18] Q. Ma, Y. Ma, X. Gong, and D. Zhang, "Improvement of tissue harmonic imaging using the pulse-inversion technique." *Ultrasound Med. Biol.*, vol. 31, no. 7, pp. 889–894, Jul 2005.

[19] J. M. Rau, S.-E. Måsøy, R. Hansen, B. Angelsen, and T. A. Tangen, "Methods for reverberation suppression utilizing dual frequency band imaging." *J. Acoust. Soc. Am.*, vol. 134, no. 3, pp. 2313–25, Sep. 2013.

[20] M. Fink, "Time reversal of ultrasonic fields – part I : basic principles," *IEEE Trans. Ultrason., Ferroelec. Freq. Contr.*, vol. 39, no. 5, pp. 555–566, 1992.

[21] B. Osmanski, G. Montaldo, M. Tanter, and M. Fink, "Aberration correction by time reversal of moving speckle noise." *IEEE Trans Ultrason Ferroelectr Freq Control*, vol. 59, no. 7, pp. 1575–83, 2012.

[22] M. Tanter, J.-l. Thomas, and M. Fink, "Focusing and steering through absorbing and aberrating layers: Application to ultrasonic propagation through the skull," *Journal of the Acoustical Society of America*, vol. 103, no. 5, pp. 2403–2410, 1998.

[23] S. P. Näsholm, R. Hansen, S.-E. Måsøy, T. F. Johansen, and B. A. Angelsen, "Transmit beams adapted to reverberation noise suppression using dual-frequency SURF imaging." *Ultrasonics, Ferroelectrics and Frequency Control, IEEE Transactions on*, vol. 56, no. 10, pp. 2124–33, Oct. 2009.

[24] R. Hansen, S.-E. Må soy, T. F. Johansen, and B. a. Angelsen, "Utilizing dual frequency band transmit pulse complexes in medical ultrasound imaging." *J. Acoust. Soc. Am.*, vol. 127, no. 1, pp. 579–87, Jan. 2010.

[25] S. P. Näsholm, R. Hansen, and B. Angelsen, "Post-Processing Enhancement of Reverberation-Noise Suppression in Dual Frequency SURF Imaging," *Ultrasonics, Ferroelectrics and Frequency Control, IEEE Transactions on*, vol. 58, no. 2, pp. 338–348, 2011.

[26] J. Camacho, M. Parrilla, and C. Fritsch, "Phase coherence imaging." *IEEE transactions on ultrasonics, ferroelectrics, and frequency control*, vol. 56, no. 5, pp. 958–74, May 2009.

[27] M. a. Lediju, G. E. Trahey, B. C. Byram, and J. J. Dahl, "Short-lag spatial coherence of backscattered echoes: imaging characteristics." *IEEE transactions on ultrasonics, ferroelectrics, and frequency control*, vol. 58, no. 7, pp. 1377–88, Jul. 2011.

[28] J. Dahl, M. Jakovljevic, G. F. Pinton, and G. E. Trahey, "Harmonic spatial coherence imaging: an ultrasonic imaging method based on backscatter coherence." *Ultrasonics, Ferroelectrics and Frequency Control, IEEE Transactions on*, vol. 59, no. 4, pp. 648–659, Apr 2012.

[29] M. Jakovljevic, G. E. Trahey, R. C. Nelson, and J. J. Dahl, "In vivo application of short-lag spatial coherence imaging in human liver." *Ultrasound Med. Biol.*, vol. 39, no. 3, pp. 534–542, Mar 2013.

[30] B. Byram and M. Jakovljevic, "Ultrasonic multipath and beamforming clutter reduction: a chirp model approach." *Ultrasonics, Ferroelectrics and Frequency Control, IEEE Transactions on*, vol. 61, no. 3, pp. 428–40, Mar. 2014.

[31] S. M. Kay, *Fundamentals of statistical signal processing: estimation theory*. Upper Saddle River, NJ, USA: Prentice-Hall, Inc., 1993.

[32] R. F. Wagner, S. W. Smith, J. M. Sandrik, and H. Lopez, "Statistics of Speckle in Ultrasound B-Scans," *IEEE Trans. Sonics and Utrasonics*, vol. 30, pp. 156–163, 1983.

[33] A. R. Selfridge, G. S. Kino, and B. T. Khuri-Yakub, "A theory for the radiation pattern of a narrow-strip acoustic transducer," *Applied Physics Letters*, vol. 37, no. 1, p. 35, 1980.

[34] X. Lv, G. Bi, C. Wan, and M. Xing, "Lv's Distribution: Principle, Implementation, Properties, and Performance," *IEEE Trans Sig Proc*, vol. 59, no. 8, pp. 3576–3591, 2011.

[35] H. Zou and T. Hastie, "Regularization and variable selection via the elastic net," *Journal of the Royal Statistical Society: Series B (Statistical Methodology)*, vol. 67, no. 2, pp. 301–320, Apr. 2005.

[36] J. Friedman, T. Hastie, and R. Tibshirani, "Regularization paths for generalized linear models via coordinate descent," *Journal of Statistical Software*, vol. 33, no. 1, pp. 1–22, 2010.

[37] R. J. Tibshirani and J. Taylor, "Degrees of freedom in lasso problems," *The Annals of Statistics*, vol. 40, no. 2, pp. 1198–1232, Apr. 2012.

[38] X. Liu, Z. Wen, and Y. Zhang, "Limited memory block krylov subspace optimization for computing dominant singular value decompositions," *SIAM Journal on Scientific Computing*, vol. 35, no. 3, pp. A1641–A1668, 2013.

[39] B. Yang, "A Study of Inverse Short-Time Fourier Transform," *IEEE International Conference on Acoustics, Speech and Signal Processing, 2008*, pp. 3541–3544, 2008.

[40] J. A. Jensen, "A model for the propagation and scattering of ultrasound in tissue," *Journal of the Acoustical Society of America*, vol. 89, no. 1, pp. 182–190, Jan. 1991.

[41] J. A. Jensen and N. B. Svendsen, "Calculation of pressure fields from arbitrarily shaped, apodized, and excited ultrasound transducers," *IEEE Trans. Ultrason., Ferroelec., Freq. Contr.*, vol. 39, pp. 262–267, 1992.